Catalysis Science & Technology

ROYAL SOCIETY OF CHEMISTRY

PAPER

View Article Online
View Journal

Cite this: DOI: 10.1039/d5cy01572c

Operando exsolved $FeNi_3$ nanoparticles for boosting ethanol internal reforming in solid oxide fuel cells

J. Roelf F. Maring, [a] Emerson L. dos Santos Veiga,[b] Francisco F. Tabuti, [b] Majid Ahmadi, [c] Fabio C. Fonseca [b] and Vasileios Kyriakou *[a]

Direct ethanol solid oxide fuel cells (SOFCs) are considered promising for power generation with high efficiency and flexibility from sustainable sources. Among their major challenges is the choice of catalytically active, chemically stable and coking tolerant fuel electrodes (anodes) for the internal reforming and oxidation of ethanol. Here, we *operando* exsolved $FeNi_3$ nanoparticles from a Ni-doped SFM ($Sr_2Fe_{1.3}Mo_{0.5}Ni_{0.2}O_{6\pm\delta}$, SFMNi) fuel electrode that significantly enhanced the power output. Our analysis confirmed that Ni doping increased surface basicity and oxygen vacancy concentration which are linked to ethanol steam reforming selectivity toward dehydrogenation pathways over the undesired dehydration observed for the undoped SFM sample. The thermocatalytic studies revealed the high ethanol reforming activity of $FeNi_3$ nanoparticles with intriguing coking tolerance properties as confirmed by crystallographic and Raman analyses. This resulted in a >30% enhancement in the peak power density with adequate stability. Our findings highlight the strong coupling between reforming activity and electrochemical performance, positioning the use of nanoparticle-functionalized perovskite electrodes as a promising strategy for efficient and flexible SOFCs operating on renewable fuels.

Received 20th December 2025,
Accepted 11th May 2026

DOI: 10.1039/d5cy01572c

rsc.li/catalysis

Introduction

International shipping emitted approximately 1.1 million tonnes of CO_2, accounting for around 2.9% of global anthropogenic greenhouse gas emissions.[1] As maritime trade continues to expand, scalable low-carbon propulsion technologies are urgently required. Fuel cells are electrochemical energy conversion devices that directly transform chemical energy into electrical energy with high efficiency, low noise, and minimal environmental impact, as they operate with no mechanical parts and do not produce air pollutants (NO_x, SO_2, particulate matter).[2]

Their operating temperature depends on the type of cell. Proton exchange membrane fuel cells (PEMFCs) operate at low temperatures and offer high current densities, but rely on expensive noble metal catalysts due to their acidic environment.[3] They are also sensitive to impurities in the fuel stream, requiring a highly purified input.[4] SOFCs, on the other hand, operate at high temperatures (700–1000 °C), which allow for internal reforming, compatibility with a wide range of fuels including hydrocarbons and alcohols, and improved electrode kinetics.[5] In SOFCs, hydrogen is the typically employed fuel which is introduced and subsequently oxidized at the anode (fuel electrode) by oxide ions migrating through the ceramic electrolyte by the reduction of molecular oxygen at the cathode (air electrode).

Although, hydrogen exhibits significant advantages and can be efficiently utilized in SOFCs, it's low volumetric energy density necessitates high-pressure or cryogenic storage, for which the required infrastructure remains underdeveloped and cost-intensive.[6] Alternatively, hydrogen containing fuels such as ammonia, methanol, and ethanol can be produced in a sustainable and efficient manner and may offer greater compatibility with existing fuel handling and storage systems.[5] Among these, ethanol originating from biobased processes, including that derived from second-generation lignocellulosic biomass, stands out as an intriguing option. Bioethanol is renewable, non-toxic, non-corrosive, and has a high volumetric energy density in liquid form under ambient conditions, facilitating storage and distribution using established infrastructure.

To utilize ethanol in SOFCs, two possible pathways are considered, either through direct electrochemical oxidation (eqn (1)) or *via* internal reforming into hydrogen (eqn (4)),

[a] *Engineering and Technology Institute Groningen (ENTEG), University of Groningen, Nijenborgh 3, 9747 AGGroningen, The Netherlands. E-mail: v.kyriakou@rug.nl*
[b] *Nuclear and Energy Research Institute (IPEN-CNEN), São Paulo, SP 05508-000, Brazil*
[c] *Zernike Institute for Advanced Materials, University of Groningen, Nijenborgh 3, Groningen, AG 9747, The Netherlands*

which is subsequently oxidized on the anodic electrode surface (eqn (6)):[7]

Direct ethanol oxidation:

$$C_2H_5OH + 6O^{2-} \rightarrow 3H_2O + 2CO_2 + 12e^- \quad (1)$$

Oxygen reduction reaction (ORR):

$$3O_2 + 12e^- \rightarrow 6O^{2-} \quad (2)$$

$$C_2H_5OH + 3O_2 \rightarrow 3H_2O + 2CO_2 \quad (3)$$

Ethanol steam reforming (ESR):

$$C_2H_5OH + 3H_2O \rightarrow 6H_2 + 2CO_2 \quad (4)$$

Hydrogen oxidation reaction (HOR):

$$H_2 + O^{2-} \rightarrow H_2O + 2e^- \quad (5)$$

$$H_2 + \frac{1}{2}O_2 \rightarrow H_2O \quad (6)$$

In the case of direct ethanol SOFCs (DESOFCs), the pathway is limited by the sluggish kinetics due to the complex 12 electron transfer process required for the complete oxidation, resulting in relatively low open-circuit voltages (OCVs) of ~0.8 V and moderate peak power densities in the range of 50–300 mW cm^{-2}.[8–12] Moreover, incomplete oxidation often leads to the formation of intermediate species such as acetaldehyde and ethylene, which can promote carbon deposition and accelerate anode degradation.[8–12]

Internal ethanol reforming SOFCs rely on anodic electrocatalyst materials to efficiently convert ethanol and steam into hydrogen and carbon dioxide. Due to the hydrogen presence instead of ethanol, higher OCVs (>1.0 V) and higher peak power densities than those of DESOFCs are enabled, hence supporting the development of more compact and lightweight SOFC systems. It is obvious that the performance is directly linked to the higher electrochemical activity of hydrogen relative to ethanol. Such behavior has previously been reported in ethanol-fueled SOFCs, where higher operating temperatures promoted ethanol decomposition, resulting in increased hydrogen formation and enhanced power densities.[13–16] The same result can be also obtained when catalytically active electrodes for ethanol reforming are employed to allow for similar hydrogen production rates without the requirement of elevated operating temperatures, which may decrease the lifetime of SOFCs.[12,17]

Nickel–yttria-stabilized zirconia (Ni–YSZ cermet) is a state-of-the-art anode material with adequate catalytic activity for hydrogen oxidation, electrical conductivity, and thermal compatibility with a ceramic electrolyte.[18] However, Ni–YSZ suffers from poor redox stability due to Ni coarsening and displays less fuel flexibility, as it is prone to coking when fed with hydrocarbons such as ethanol.[19] On the other hand, perovskite oxides have emerged as promising alternative anode materials due to their mixed ionic-electronic conductivity (MIEC), high redox stability, and in the case of some specific compositions, enhanced tolerance to diverse fuels.[14,20,21]

The catalytic performance of SOFC anodes can be further improved through the incorporation of metal nanoparticles *via* infiltration[22] or exsolution.[23] Infiltration deposits catalytic metal nanoparticles onto the anode surface, increasing activity, but often suffers from particle agglomeration and limited thermal stability during prolonged operation. Conversely, exsolution generates metal nanoparticles that are socketed to the perovskite backbone, resulting in enhanced thermal stability, sintering resistance, and durability.[24] Efficient cleavage of C–C bonds is critical for converting ethanol into hydrogen and CO.[20] Both infiltration and exsolution facilitate this process, but exsolved nanoparticles typically provide better control over particle size and distribution,[25] which is essential for effective reforming and carbon deposition resistance.

Molybdenum-doped strontium ferrites ($Sr_{2.0}Fe_{1.5}Mo_{0.5}O_{6\pm\delta}$, SFM) have attracted significant research attention as fuel electrodes for hydrogen oxidation, steam and/or CO_2 electrolysis in solid oxide reactors[26–28] due to their significant MIEC properties.[29] Concurrently, various B-site doping strategies have been followed to achieve exsolution of catalytically active nanoparticles at the host SFM.[27,28,30,31] Here, we have employed a Ni-doped SFM ($Sr_2Fe_{1.3}Mo_{0.5}Ni_{0.2}O_{6\pm\delta}$, SFMNi) that allows the *operando* exsolution of Ni–Fe nanoparticles under the reducing conditions induced by ethanol steam reforming (ESR). This approach eliminates the need for a separate pre-reduction step and yields Ni–Fe particles that modify the surface chemistry, shifting selectivity from ethanol dehydration to dehydrogenation. The *in situ* generated hydrogen over Ni–Fe nanoparticles on the SFMNi fuel electrode reduces polarization resistance during SOFC operation and enhances power density compared to direct ethanol oxidation on SFM electrodes lacking catalytically active exsolved nanoparticles. These findings indicate that exsolved nanoparticles enable endothermic ethanol reforming, thereby achieving higher SOFC performance and supporting more compact SOFC designs.

Experimental

Electrode preparation

$Sr_{2.0}Fe_{1.5}Mo_{0.5}O_{6\pm\delta}$ (SFM) and $Sr_{2.0}Fe_{1.3}Mo_{0.5}Ni_{0.2}O_{6\pm\delta}$ (SFMNi) were synthesized *via* a modified sol–gel method using EDTA and citric acid as chelating agents. Stoichiometric amounts of $Sr(NO_3)_2$, $Fe(NO_3)_2{\cdot}9H_2O$, $(NH_4)_6Mo_7O_{24}{\cdot}4H_2O$ and $Ni(NO_3)_2$ were dissolved in Milli-Q water containing EDTA and citric acid at a molar ratio of 1 : 1 : 1.5 (metal ions : EDTA : citric acid). The pH was adjusted to 9 using 25% NH_3-H_2O. After complete dissolution, the solution was heated to 90 °C under continuous stirring for 2 h to form a gel, which was subsequently combusted at 300 °C for 2 h (5 °C min^{-1}). The resulting ash was

ground and calcined at 1100 °C for 5 h (2 °C min^{-1}) to obtain the final perovskite powders.

Scandia-stabilized zirconia (ScSZ) electrolyte substrates, gadolinium-doped ceria powder ($Gd_{0.1}Ce_{0.9}O_{1.95}$, GDC mid-grade), lanthanum strontium cobalt ferrite powder ($(La_{0.6}Sr_{0.4})_{0.95}Co_{0.20}Fe_{0.80}O_{3-\delta}$, LSCF-P), screenprint ink (α-terpineol) and gold paste were purchased from Fuel Cell Materials and used for cell fabrication. Electrolyte-supported cells with the configuration Au/SFM(Ni)-GDC/GDC/ScSZ/GDC/LSCF-GDC/LSCF were fabricated using ScSZ substrates (Fuel Cell Materials, 211214) with a 25 mm diameter and 150 μm nominal thickness. A GDC barrier layer (50 : 50 wt% solids:α-terpineol, 2 $mg_{calcined}$ cm^{-2}) was screen printed onto both sides of the electrolyte and sintered at 1300 °C for 4 h (2 °C min^{-1}), yielding a dense layer that prevented insulating interfacial phases and improved adhesion *via* enhanced surface roughness. A functional LSCF-GDC (50 : 50 wt%) layer (35 : 65 wt% solids : α-terpineol, 4 $mg_{calcined}$ cm^{-2}) and an LSCF current collector layer (30 : 70 wt% solids : α-terpineol, 4 $mg_{calcined}$ cm^{-2}) were sequentially screen printed on top. On the anode side, a functional SFM-GDC or SFMNi-GDC layer (35 : 65 wt% solids : α-terpineol, 4 $mg_{calcined}$ cm^{-2}) was applied on the GDC barrier. The complete cell was sintered at 1100 °C for 2 h with a heating rate of 2 °C min^{-1}. Gold paste was applied to the sintered anode for current collection and heated at 300 °C for 2 h to remove organic residues. Gold was assumed to be electrochemically inert towards hydrogen and ethanol oxidation. The geometric active cell area was 1 cm^2.

Characterisation

Structural bulk properties and phase purity were examined by powder X-ray diffraction (Bruker D8 Endeavor) using Cu $K_{\alpha1}$ (λ = 1.5406 Å) and Cu K_β (λ = 1.392 Å) radiation at 40 kV and 25 mA. Diffraction data were collected over a 2θ range of 20–80° with a scan rate of 1° min^{-1}. Elemental analysis by inductively coupled plasma optical emission spectrometry (ICP-OES) was performed using a PerkinElmer Optima 7000 DV instrument to determine the elemental concentration of the as-prepared SFM-based materials.

X-ray photoelectron spectroscopy. X-ray photoelectron spectroscopy (XPS) measurements were performed using a Thermo Scientific ESCALAB 250Xi equipped with a monochromatic aluminum source (Kα = 1486.6 eV). The analysis area was defined by a 650 μm spot size, with the X-ray source operated at 14.8 kV and 1.6 A. Survey spectra were collected with a pass energy of 100 eV and a step size of 1 eV, while high-resolution spectra were acquired with a pass energy of 20 eV and a step size of 0.1 eV. Charge compensation was applied by referencing the adventitious carbon C 1s peak to 284.8 eV. The spectra were processed using Thermo Avantage software, including background subtraction and peak fitting.

NH_3-TPD and CO_2-TPD measurements were carried out using an Autochem II 2920 instrument from Micromeritics. Prior to analysis, the samples (0.1 g) were pretreated at 400 °C for 60 min under a 30 sccm He flow. For NH_3-TPD, the samples were cooled to 100 °C, exposed to a 10% NH_3-He stream (30 sccm) for 60 min to saturate the surface, and then analyzed by heating from 100 to 850 °C at a rate of 10 °C min^{-1} under pure He (30 sccm). For CO_2-TPD, the same pretreatment was applied, after which the samples were cooled to 100 °C, saturated with pure CO_2 (30 sccm) for 60 min, and subsequently analyzed from 100 to 850 °C at a rate of 10 °C min^{-1} under pure He (30 sccm). The oxygen release from the as-prepared materials was analyzed on a Perkin Elmer TGA 4000 (Perkin Elmer, Waltham, MA, USA). TGA analyses were performed within a temperature range of 50–850 °C (heating rate: 10 °C min^{-1}) in air. The oxygen vacancies of the samples were evaluated by electron paramagnetic resonance (EPR) on a Bruker A300 spectrometer at room temperature and in an air environment.

Electrode microstructures and spent catalyst surfaces were characterized by scanning electron microscopy (FEI Nova NanoSEM 650). Raman spectroscopy was employed to probe structural and vibrational characteristics of the samples. Spectral acquisition utilized a Horiba XploRA-PLUS confocal Raman system featuring a 532 nm excitation source and 50× objective lens. Measurements covered the 200–1200 cm^{-1} spectral region with a spectral resolution of 2–3 cm^{-1}. All spectra underwent processing and analysis through the LabSpec6 analytical platform.

The microstructure of the samples was examined with a double-corrected (probe and image correctors) and monochromated Themis Z scanning transmission electron microscope (Thermo Fisher Scientific) operating at 300 kV. The STEM images were acquired through HAADF (high-angle annular dark-field) mode, and TEM images were captured using a Ceta 16M camera. The beam convergence angle was measured ~24 mrad, and the probe current of 30–50 pA was used for STEM imaging. The TEM samples were prepared by drop-casting an ethanol suspension of the catalyst onto lacey carbon-supported copper grids, followed by transfer into the microscope using a specialized double-tilt holder optimized for X-ray collection.

Energy dispersive X-ray spectroscopy (STEM EDS maps) results were achieved with a Dual X EDS system (Bruker) using two large area detectors in total capturing 1.76 steradian with a probe current of 50 pA for more than 2 hours. Data acquisition and analysis were done using Velox software.

Thermocatalytic evaluation

Catalytic performance was evaluated in a fixed-bed quartz reactor (U-tube configuration, 6 mm of internal diameter) containing 20 mg of catalyst. The furnace temperature was increased to the reaction temperature under pure N_2 (60 mL min^{-1} flow rate). The ESR experiments were performed at 700 °C and 750 °C with a feed composition of a H_2O : EtOH molar ratio of 4 : 1 (2.6% EtOH–10.4% H_2O-N_2), selected to favour the water–gas shift reaction. Ethanol and

water vapours were delivered to the reactor using two independent N_2 carrier streams (each at 30 mL min^{-1}), saturated by passing through temperature-controlled saturators (20 °C for ethanol, 59 °C for water). Analysis of the reactor effluent was conducted using an Agilent 7890A gas chromatograph. This instrument incorporated both a flame ionization detector (FID) and a thermal conductivity detector (TCD), coupled to molecular sieve and Plot U columns for gas separation. Ethanol conversion ($X_{ethanol}$) and product formation rates (R_x) were determined using eqn (7) and eqn (8), respectively.

These calculations employed the inlet and outlet molar ethanol flow rates ($F_{ethanol,in}$ and $F_{ethanol,out}$), the total molar flow rate (F_{total}), the catalyst bed mass (m_{cat}), and the molar fraction of each product species (y_x):

$$X_{ethanol} = \frac{F_{Ethanol,in}}{F_{Ethanol,out}} \cdot 100 \quad (7)$$

$$R_x = \frac{F_{total} \cdot y_x}{m_{cat}} \quad (8)$$

Electrochemical characterisation

Electrochemical measurements were performed using an Open Flanges™ setup (Fiaxell Sàrl), enabling reproducible testing without ceramic sealing paste. The anode chamber was sealed by compressing the cell onto a mica ring (Thermiculite® 870, Flexitallic), while the cathode remained open to ambient air. Current collection from the anode was achieved through a gold mesh placed beneath the cell within the mica ring. A gold M_Grid™, connected to two gold wires, served as the current collector for the cathode. The wires were insulated with alumina felt to prevent short circuits. The assembly was enclosed between a Crofer 22 APU gas diffusion plate (anode) and a stainless-steel gas diffusion plate (cathode), each equipped with welded inlet/outlet tubes for gas distribution. Uniform compression was applied using four springs.

A Zahner IM6 Electrochemical Workstation was used to conduct electrochemical measurements. Linear sweep voltammetry was conducted from OCV to 0.2 V at a scan rate of 10 mV s^{-1}. Electrochemical impedance spectroscopy (EIS) was recorded at 0.6 V under fuel cell conditions, using a frequency range of 100 kHz to 0.1 Hz and a 10 mV AC perturbation. Cell stability was evaluated by monitoring the current response at a constant voltage of 0.6 V. All measurements were conducted at 750 °C, with the temperature monitored *via* type-K thermocouples embedded in the stainless-steel diffusion plate in contact with the cell. Air was supplied to the cathode to maintain the oxidized state of the LSCF electrode. Steam was generated by bubbling N_2 through a water reservoir maintained at 55 °C. Ethanol was introduced by bubbling a separate N_2 stream through an ethanol reservoir at 29 °C, yielding an ethanol-to-steam molar ratio of 1 : 4. All gas lines were heated to 120 °C to prevent condensation.

Results and discussion

Characterisation of the as-prepared samples

The composition $Sr_{2.0}Fe_{1.3}Ni_{0.2}Mo_{0.5}O_{6\pm\delta}$ (SFMNi) was selected alongside $Sr_{2.0}Fe_{1.5}Mo_{0.5}O_{6\pm\delta}$ (SFM), since Ni = 0.2 doping has been reported to yield optimal nanoparticle dispersion and stability.[27,28,31] The crystal structure and purity of the as-prepared SFM and SFMNi were confirmed by XRD and ICP-OES analysis (Fig. 1a and b). The results revealed that pure perovskite phases were achieved for both samples following the calcination process in ambient air at 1100 °C for 5 h. The magnified section of the XRD pattern indicate a shift of SFMNi to higher 2θ angles compared to SFM, implying a decrease in lattice cell volume upon Ni doping. More specifically, in SFM, the oxidation state of Fe is a mixture of Fe^{2+} (0.78 Å) and Fe^{3+} (0.645 Å) and the direct substitution of Fe^{2+} with a Ni^{2+} ion (0.69 Å) could partially explain this observation. In addition, when Ni^{2+} is incorporated into the structure, Fe and Mo tend to attain higher oxidation states to maintain charge balance, thus also decreasing the cell volume.[32] By carrying out XPS analysis on the samples, an increased fraction of Fe^{3+} over Fe^{2+} species for SFMNi was observed due to the positive shift of the $Fe2p_{3/2}$ peak toward higher binding energies upon Ni doping (Fig. 1c).[11] A similar effect is also observed for the Mo $3d_{5/2}$ peak, where a positive shift to higher binding energies shows an increased fraction of Mo^{6+} (0.59 Å) relative to Mo^{5+} (0.61 Å) (Fig. 1d).[11] These findings indicate that Ni doping decreases the ratio of Fe^{2+}/Fe^{3+} and Mo^{5+}/Mo^{6+} couples, leading to lattice shrinkage as reported for B-site cations in other perovskite systems.[33,34] Furthermore, XPS analysis of the Sr 3d, O 1s and C 1s regions reveals that the as-prepared SFM surface is more extensively hydroxylated and carbonated than the as-prepared SFMNi (Fig. S1). The positive binding energy Sr 3d shift, strong O 1s ~530.5 eV peak region, and C 1s peak at ~289 eV indicate a hydroxyl carbonate-rich surface on SFM,[35] while SFMNi shows a lower oxygen-to-cation ratio (1.38 *vs.* 2.05), implying higher oxygen vacancy concentration on the as-prepared SFMNi.[36]

Surface acidity and oxygen defect chemistry strongly influence product selectivity during ESR. Ethanol dehydration to ethylene is promoted on acidic sites, whereas dehydrogenation to acetaldehyde is favored on basic sites.[37] Since ethylene readily leads to coking through oligomerization, the dehydrogenation pathway is generally preferred to stabilize ESR performance. To assess surface acid–base properties, CO_2-TPD and NH_3-TPD measurements were carried out on the SFM and SFMNi samples and the results are shown in Fig. 2. CO_2-TPD (Fig. 2a) revealed a higher CO_2 adsorption capacity for SFMNi, indicative of increased basicity, whereas NH_3-TPD (Fig. 2b) showed stronger acidity for SFM relative to SFMNi. The integrated peak areas are summarized in Table 1, demonstrating the higher ratio of base to acid sites for SFM. This suggests that SFM may exhibit a stronger preference for ethanol dehydration over dehydrogenation compared to SFMNi. Ni doping may modify the effective surface charge, whereby acid

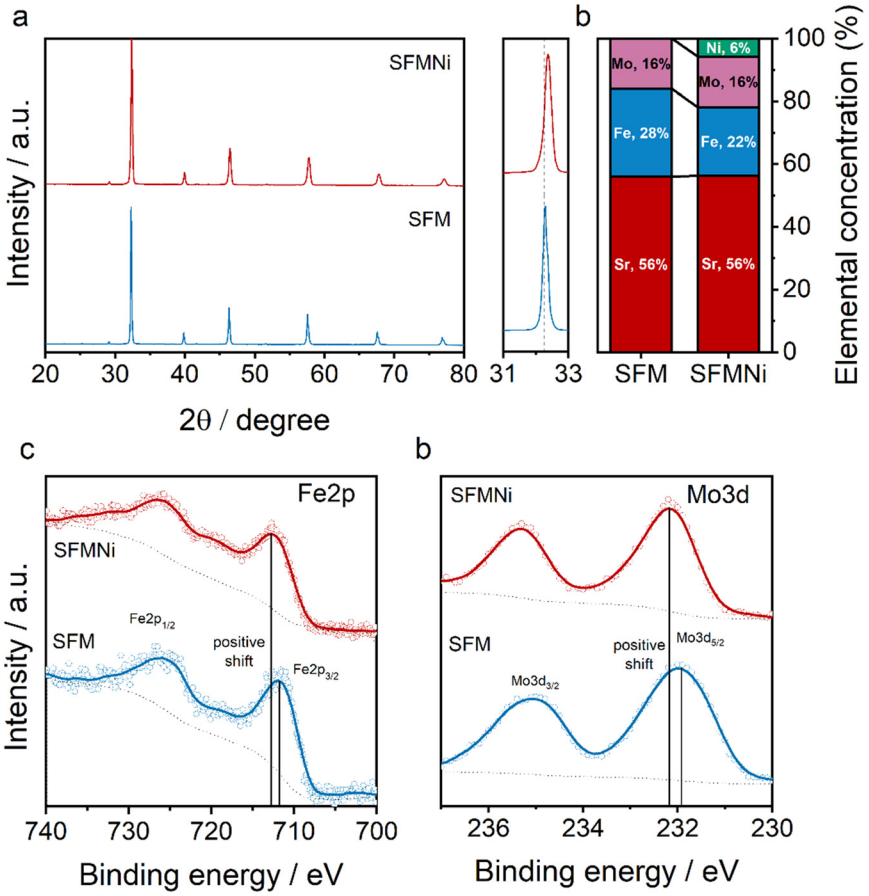

Fig. 1 Crystallographic and compositional characterization of the as-prepared SFM and SFMNi. (a) XRD patterns showing the effect of Ni doping, with a magnified region around 32° highlighting a rightward shift to higher angles, and (b) elemental weight fractions determined by ICP-OES. XPS spectra of the as-prepared SFM and SFMNi of (c) Fe 2p and (d) Mo 3d regions showing a positive shift in binding energy after Ni doping.

strength correlates with the density of positively charged sites, while basic strength is associated with negatively charged surface species.[38] While this may be evaluated by XPS, the positive shifts toward higher binding energy of the Fe 2p and Mo 3d spectra indicate the presence of more positively charged metal centers on the as-prepared SFMNi in comparison to the as-prepared SFM. This suggests that acidity measured through NH_3-TPD may not primarily originate from a difference in cation oxidation states. However, discrepancies may arise from differences in measurement conditions between desorption techniques and XPS. Furthermore, it should be noted that conventional XPS probes several nanometers into the material and may therefore not accurately represent the composition of the outermost catalytic monolayers.[39]

Low-temperature EPR was employed to quantify oxygen vacancies in the as-prepared SFM and SFMNi, revealing a characteristic signal at a *g*-factor of 2.001 (Fig. 2c). The higher intensity observed for SFMNi indicates that Ni incorporation promotes additional oxygen vacancy formation. This observation is further supported by TGA (Fig. 2d), where the greater weight loss between 50 and 850 °C corresponds to the release of adsorbed species and lattice oxygen. Collectively, these results demonstrate that SFMNi exhibits an increased concentration of oxygen vacancies compared to SFM, suggesting reduced susceptibility to carbon deposition and promoted steam activation.[37]

Catalytic testing

The thermocatalytic performance of SFM and SFMNi powders was assessed in an ethanol–steam mixture (2.6% EtOH–10.4% H_2O-N_2) at 700 and 750 °C to examine the influence of operating temperature on exsolution behavior and to identify the optimal conditions for SOFC operation (Fig. 3). Excess steam was selected to shift the water–gas-shift equilibrium to hydrogen formation. SFM demonstrates similar ESR performance at both 700 and 750 °C, achieving ~29% ethanol conversion after 20 h on stream and producing 1.04 and 1.08 mol min^{-1} g_{cat}^{-1} of H_2 and 0.76 and 0.79 mol min^{-1} g_{cat}^{-1} of acetaldehyde, respectively (Fig. 3a and b). Furthermore, small amounts of ethylene were observed at both 700 and 750 °C over the course of time with 0.184 and 0.222 mol min^{-1} g_{cat}^{-1}, respectively. The low ESR activity is attributed to the absence of a metallic phase, which limits C–C bond cleavage. Consequently, hydrogen, acetaldehyde and ethylene are mainly detected in the outlet, indicating

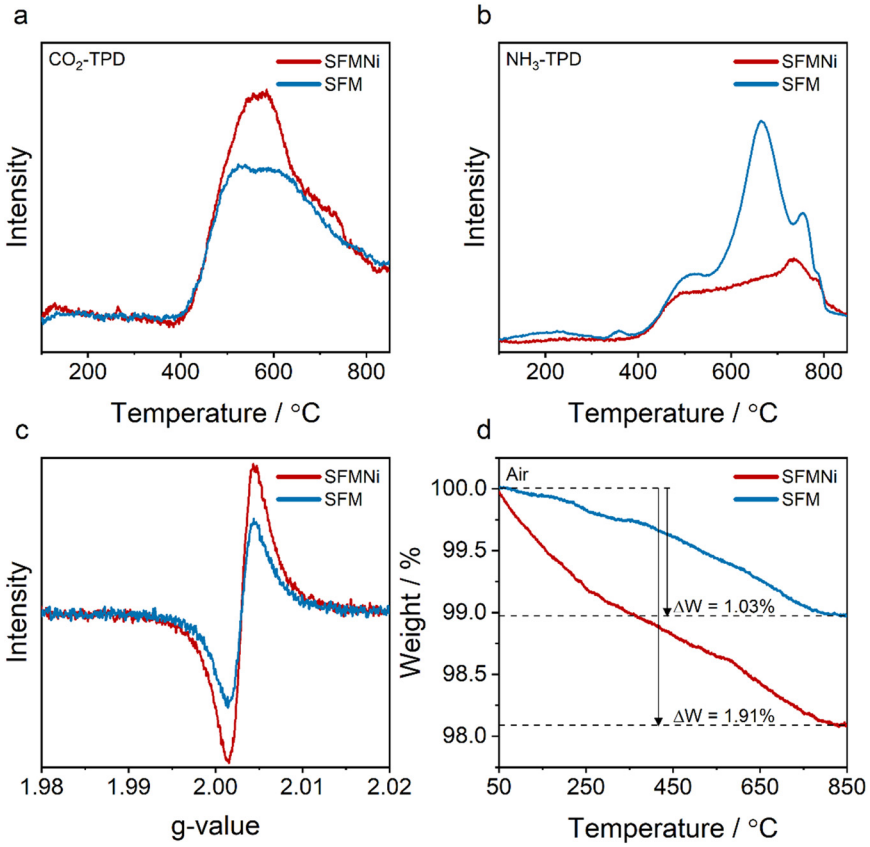

Fig. 2 Characterization of surface acidity and oxygen vacancy capacity of the as-prepared SFM and SFMNi samples. (a) CO_2-TPD profiles demonstrating surface basicity, (b) NH_3-TPD profiles identifying the surface acidity, (c) TGA curves in air indicative of oxygen release, and (d) EPR spectra highlighting the relative concentration of bulk oxygen vacancies.

Table 1 Density of base and acid sites on the as-prepared SFM and SFMNi powders

	Base sites μmol g^{-1}	Acid sites μmol g^{-1}	Ratio of base to acid sites
SFM	201.31	613.77	3.05
SFMNi	293.56	364.88	1.24

that ethanol dehydrogenation and dehydration are dominant (eqn (9) and (10)):

$$C_2H_5OH \rightarrow CH_3CHO + H_2 \quad (9)$$

$$C_2H_5OH \rightarrow C_2H_4 + H_2O \quad (10)$$

In contrast, the SFMNi sample exhibited improved catalytic activity at 700 °C compared to SFM (Fig. 3). After 20 h, the ethanol conversion reached 44%, while the dominant products were measured to be acetaldehyde (1.54 mol min^{-1} g_{cat}^{-1}), hydrogen (2.74 mol min^{-1} g_{cat}^{-1}), CO (0.48 mol min^{-1} g_{cat}^{-1}) and to a lesser extent ethylene (0.168 mol min^{-1} g_{cat}^{-1}). Minor CO formation indicates limited ethanol steam reforming and a weak contribution from metallic sites, confirming ethanol dehydrogenation as the dominant pathway (eqn (9)). The enhanced activity may be attributed to Ni doping, facilitating oxygen vacancy formation under reductive conditions and increasing surface basicity for ethanol dehydrogenation.[27,40,41]

At 750 °C, SFMNi exhibits significantly enhanced ESR activity, achieving complete ethanol conversion over the course of 20 h (Fig. 3). During the initial reaction hours, H_2 and CO production increase and stabilize at 18.1 and 6.1 mol min^{-1} g_{cat}^{-1}, respectively, indicating that ESR is the dominant pathway. During the 20 h experiment, only minor traces of ethylene were detected, while acetaldehyde was completely absent. This suggest that the sites enable efficient C–C bond cleavage of ethylene and acetaldehyde to produce H_2 and CO. The low CO_2 formation indicates a negligible contribution from the water–gas shift reaction, consistent with its exothermic nature being thermodynamically disfavored at elevated temperatures. This reveals an untapped potential for additional hydrogen formation, which could be enabled by

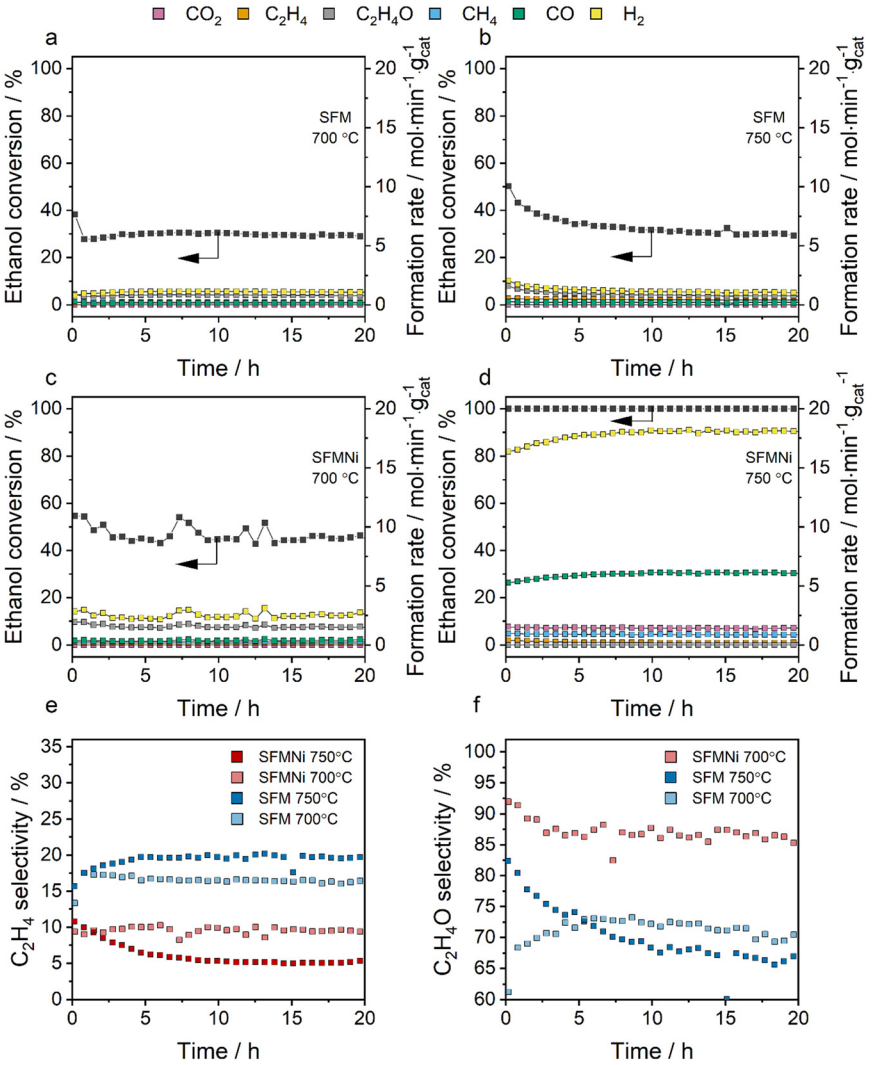

Fig. 3 Ethanol conversion, product formation rates and selectivity during ESR (2.6% EtOH–10.4% H_2O-N_2). (a) SFM at 700 °C, (b) SFM at 750 °C, (c) SFMNi at 700 °C, and (d) SFMNi at 750 °C, illustrating the influence of temperature and Ni incorporation on ethanol conversion and the generation of reforming products. Influence of the catalyst and temperature on (e) ethylene (C_2H_4) and (f) acetaldehyde (C_2H_4O) selectivity, indicating the effect of surface acidity on the dehydration and dehydrogenation reaction pathway with SFMNi at 750 °C lacking C_2H_4O selectivity due to complete acetaldehyde steam reforming.

further tailoring the surface chemistry for CO adsorption and steam dissociation.[42]

The relative differences in ethylene and acetaldehyde selectivity between SFM and SFMNi are consistent with NH_3-TPD and CO_2-TPD measurements, which reveal a higher affinity of SFM for ethanol dehydration to ethylene, whereas SFMNi favors ethanol dehydrogenation (Fig. 3e and f). These results demonstrate that Ni doping modifies the surface acidity, enhancing selectivity toward acetaldehyde formation while suppressing ethylene, a known coke precursor through oligomerization.[37]

Post-testing characterization

The combined effect of high temperature, Ni doping and the reducing environment induced by ethanol reforming may drive *operando* exsolution of metallic nanoparticles facilitating efficient ESR performance. This mechanism is investigated by post-mortem XRD data (Fig. 4a and b), revealing a discrete peak at ~44° assigned to the $FeNi_3$ alloy phase after ESR at 750 °C for 20 h. HAADF-STEM characterisation combined with elemental mapping corroborates the presence of Ni–Fe alloy nanoparticles on the surface of SFMNi after ESR at 750 °C for 20 h (Fig. S3). STEM-EDX quantification of three selected areas reveals a clear difference from the total mapped area (Fig. S5). All selected areas show reduced atomic fractions of O, Sr, and Mo relative to the bulk composition, accompanied by pronounced Ni enrichment (Table S1). A slight Fe enrichment is also observed in most regions, suggesting segregation of Fe with Ni supporting the presence of the $FeNi_3$ alloy phase.

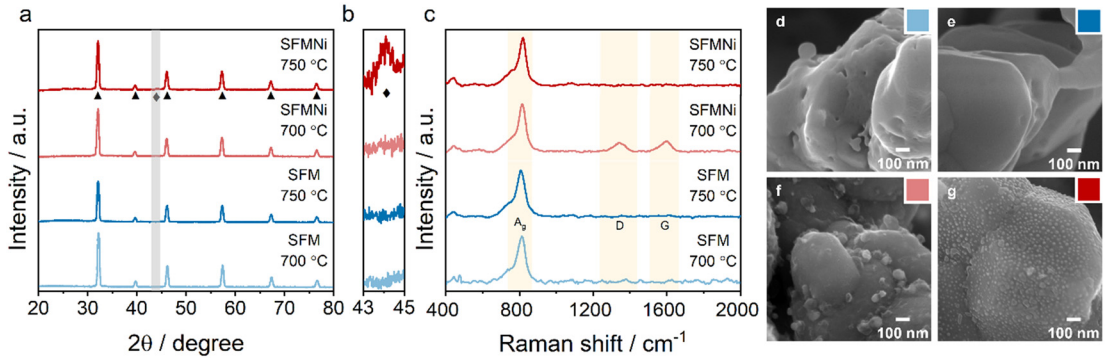

Fig. 4 Post-test crystallographic and spectroscopic characterization of spent SFM and SFMNi after ethanol-steam reforming (2.6% EtOH–10.4% H_2O-N_2) at 700 and 750 °C for 20 h. (a) XRD patterns demonstrating structural integrity of the spent powders, (b) magnified region (43–45°) highlighting the peak at 44°, indicative of Ni–Fe nanoparticle formation, (c) Raman spectra evidencing the presence or absence of carbon deposition on the spent catalyst powders and SEM imaging illustrating morphological change of (d) SFM 700 °C, (e) SFM 750 °C, (f) SFMNi 700 °C and (g) SFMNi 750 °C.

The characteristic peak at ~44° is however absent in the diffraction pattern of spent SFMNi at 700 °C, indicating that the conditions were insufficient to induce exsolution, either due to the weak reducing environment from limited ethanol dehydrogenation or the lower thermal driving force. However, lowering the temperature has been shown to generate exsolved particle size distributions advantageous for high catalytic performance.[43] Regardless of temperature, SFMNi exhibited excellent structural integrity, as evidenced by the absence of secondary peaks in the diffraction patterns. The diffraction patterns of spent SFM after ESR testing at 700 and 750 °C confirm excellent structural stability, with no detectable secondary reflections. Moreover, no reflections attributable to metallic phases were observed, indicating the absence of the key component for enhanced ESR performance.

Post-test characterization by Raman spectroscopy and SEM reveals correlated structural and morphological changes that reflect carbon tolerance and activity (Fig. 4c–f). All samples display characteristic double-perovskite modes, with a high-frequency peak near 800 cm^{-1} assigned to A_g stretching vibrations and a low-frequency peak near 750 cm^{-1} corresponding to B_g anti-stretching/bending modes.[44] SFM shows no carbon-related bands or morphological changes at either temperature, consistent with its negligible reforming activity (Fig. 4d and e). For SFMNi at 700 °C, Raman spectra show carbon-related D (~1350 cm^{-1}) and G (~1590 cm^{-1}) bands,[45] consistent with SEM evidence of surface carbon deposits (Fig. 4f),[46] indicating partial deactivation. SEM imaging reveals the presence of exsolved particles on SFMNi at 700 °C (Fig. 4f), while a distinct crystallographic signature of exsolution is not observed. This is further corroborated by back-scattered electron imaging, which provides clear Z-contrast differentiation between the support, the exsolved phase, and carbonaceous species (Fig. S2). Carbon formation appears to proceed *via* a characteristic base-growth mechanism on the exsolved nanoparticles, driven by strong metal–support interactions, rather than through the tip-growth mechanism commonly observed on deposited nanoparticles.[24] Although desorption measurements (Fig. 1) and thermocatalytic evaluation (Fig. 3) indicate higher ethanol dehydration selectivity on SFM than on SFMNi, coking observed on SFMNi suggests either the presence of an alternative coking mechanism or an increased availability of coke precursors (acetaldehyde + ethylene) due to its higher reforming activity. Nevertheless, at 750 °C, SFMNi lacks these carbon bands, instead displaying pronounced exsolved nanoparticles in SEM images (Fig. 4g), in agreement with its sustained catalytic performance.

Direct ethanol fuel cell performance

Electrochemical tests of SFM and SFMNi fuel electrode materials were conducted to evaluate the influence of exsolved Ni–Fe nanoparticles on direct ethanol SOFCs using a 2.6% EtOH–10.4% H_2O-N_2 fuel inlet at 750 °C (Fig. 5). The electrolyte-supported cell architecture (SFM(Ni)-GDC/GDC//ScSZ//GDC/LSCF-GDC/LSCF) is shown in Fig. S5. A GDC barrier layer was introduced to enhance electrode–electrolyte adhesion and suppress $SrZrO_3$ formation at the interface.[47] To further improve oxygen-ion conductivity, the fuel electrodes were prepared as SFM-GDC and SFMNi-GDC composites (see the Experimental section).[48] Cross-sectional SEM analysis of the sintered fuel cell confirmed the uniform deposition of functional layers on the ScSZ electrolyte (~153 μm thick). A dense GDC barrier layer (~5 μm) was observed at both fuel and air interfaces, confirming strong adhesion after high-temperature sintering (Fig. S5c and d). The SFMNi-GDC, LSCF-GDC and LSCF electrode layers exhibited homogeneous, highly porous microstructures with a thickness of ~12.6, 9.9 and 8.0 μm, respectively, favoring gas transport to and from the electrochemically active region. It should be noted that GDC exhibits good electrochemical performance when used as a pure anode. However, previous studies have reported that composite SFMNi-GDC electrodes outperform GDC alone.[49]

The electrochemical performance was evaluated by current voltage curves from OCV to 0.2 V and impedance spectroscopy diagrams at 0.6 V at two different time intervals at $t = 0$ (Fig. S6)

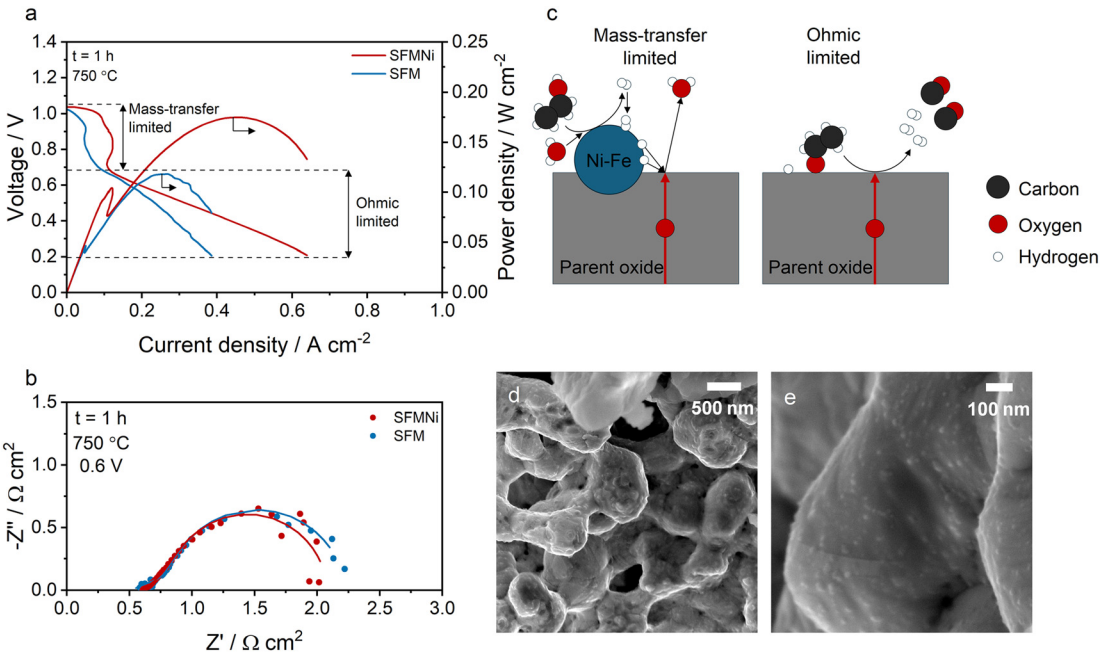

Fig. 5 SOFC performance of SFM and SFMNi fuel electrodes in an ethanol–steam atmosphere (2.6% EtOH–10.4% H_2O-N_2) at 750 °C. (a) Current–voltage and power density curves after 1 h on stream, highlighting enhanced indirect SOFC operation and increased power output due to internal reforming over exsolved Ni–Fe nanoparticles, (b) Nyquist plots recorded at 0.6 V after 1 h, illustrating resistance contributions of both cells, (c) schematic representation of the role of exsolved Ni–Fe nanoparticles in promoting internal reforming and indirect ethanol utilization and (d and e) SEM imaging on the SFMNi fuel electrode evidencing the presence of exsolved nanoparticles during ethanol fueled SOFC operation.

and t = 1 h (Fig. 5). The current–voltage (Fig. 5a) curve shows two distinct regimes: a mass-transfer limited region (from OCV to ~0.7 V) and an ohmic limited region (~0.7 to 0.2 V) controlled by charge transfer and ohmic losses. In the mass-transfer limited regime (Fig. 5a), the current is sustained by the oxidation of hydrogen from ESR, with the voltage decline in this range reflecting a mass transfer-limited regime due to hydrogen consumption and depletion. Below 0.7 V, the system transitions to an ohmic limited region, where energetics become favorable to directly oxidize ethanol and kinetics are dominated by charge transfer rather than mass transport, delivering peak power densities of 0.118 and 0.161 mW cm^{-2} for SFM and SFMNi, respectively (Fig. S6). It should be noted, however, that intermediate products such as acetaldehyde and ethylene may also be oxidized within this region.

The mass transfer-limited region in ethanol SOFCs has been attributed to hydrogen produced by the ESR thermocatalytic conversion of ethanol to hydrogen at the anode surface.[13,14] Enhancing thermocatalytic activity, either by increasing temperature or by functionalizing the perovskite surface, is therefore expected to increase hydrogen availability and improve electrochemical performance. While SFM does not undergo surface functionalization *via* redox exsolution (Fig. 4a), SFMNi has been shown to exsolve Ni–Fe nanoparticles *operando* under ethanol–steam mixtures (2.6% EtOH–10.4% H_2O-N_2). Such a feature is further confirmed by SEM imaging of an identical cell with a SFMNi fuel electrode aged in 2.6% EtOH–10.4% H_2O-N_2 for 2 h at 750 °C, evidencing the presence of nanoparticles on the surface (Fig. 5d and e). The current–voltage measurements (Fig. 5a) at t = 1 h revealed a significant change in the mass-transfer limited region for SFM and SFMNi relative to the current–voltage measurement at t = 0 (Fig. S6). Fig. S7 shows that the voltage limitation below ~0.7 V in 2.6% EtOH–10.4% H_2O-N_2 is due to limited H_2 availability, as this limitation is not observed under 97% H_2-H_2O. For the SFMNi with increased ESR performance, the hydrogen production was enhanced and the fuel cell performance at low current was significantly extended, accompanied by a local power density peak of 0.104 mW cm^{-2} at 0.86 V. By further increasing the current density, in the ohmic limited region, the peak power densities for SFM and SFMNi were 0.118 and 0.175 mW cm^{-2}, respectively. Nonetheless, SFMNi exhibits a significant enhancement compared to SFM with a considerably larger limiting current. The Nyquist plot at 0.6 V (Fig. 5c) reveals that the performance difference between SFM and SFMNi is primarily attributed to polarization resistance, R_p = 1.74 and 1.50 Ohm cm^2, respectively, rather than ohmic resistance R_0 = 0.52 and 0.61 Ohm cm^2, respectively. This is evidenced by similar first intercepts with the real axis, while the reduced second intercept for SFMNi reflecting its lower R_p. Equivalent circuit fitting parameters are summarized in Table S2. Deconvolution of R_p into two constant phase elements shows that the largest variation arises from the low-frequency resistance (R_2), corresponding to gas adsorption and surface diffusion processes.[50–52] This contribution is reduced in SFMNi, consistent with the functionalization by exsolved Ni–Fe nanoparticles. Such nanoparticles may enhance H_2 adsorption, as supported by DFT calculations indicating more favorable

energetics on the Ni(111) and Fe(110) surfaces compared to SFM(001).[53–55]

These findings highlight the potential of nanoparticle-functionalized perovskite electrodes for alcohol (or hydrocarbon)-fueled SOFC systems, as schematically illustrated in Fig. 4c. Enhanced reforming activity increases hydrogen partial pressure, thereby indirectly improving electrochemical performance. Although steam reforming is an endothermic process, the required energy can be supplied by heat, enabling efficient electricity generation at the expense of thermal energy while simultaneously achieving higher power densities and facilitating more compact, lightweight SOFC designs.

Long-term stability evaluation

The long-term stability of the SFMNi cell was evaluated at a constant voltage of 0.6 V over 168 hours (Fig. 6). The initial current density of 0.254 A cm^{-2} gradually decreased to 0.208 A cm^{-2}, primarily during the first 70 hours after which the cell stabilized reaching 0.212 A cm^{-2} at 168 h. Nyquist plots recorded at 0.6 V at different time intervals (t = 1, 70, and 168 h) reveal that the long-term degradation predominantly arises from processes in the mid- to low-frequency range (<10 Hz), while the stable first intercept with the real axis confirms an unchanged ohmic contribution of the cell (Table S2). This indicates that the degradation is not associated with the electrolyte, or contact resistance in the electrolyte/electrode interface, confirming the robustness of the cell architecture and fabrication of the electrolyte-supported cell. Similarly, the dominant variation in R_p originates from the low-frequency resistance (R_2), associated with gas adsorption and surface diffusion, suggesting that the fuel electrode suffers from carbon deposition, particle coarsening or sintering of the grain boundaries.[56] Raman analysis of the spent cell after 168 h on stream confirms carbon deposition through the appearance of the D-band (~1350 cm^{-1}) and G-band (~1590 cm^{-1}). Nevertheless, the stable current density after 70 h on stream indicates that carbon formation on the electrode surface reaches a steady state.

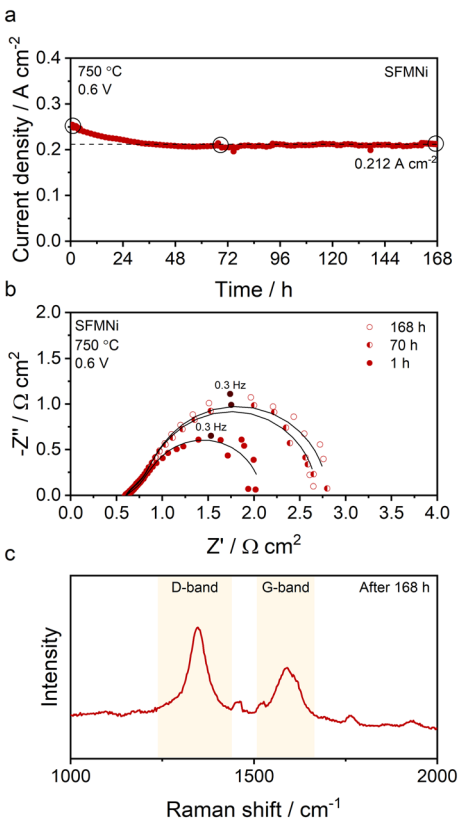

Fig. 6 Long-term stability of the SFMNi fuel electrode in an ethanol–steam atmosphere (2.6% EtOH–10.4% H_2O-N_2) at 0.6 V and 750 °C. (a) Potentiostatic performance at 0.6 V over 7 days, (b) corresponding Nyquist plots recorded after 1 h, 70 h, and 168 h, illustrating the evolution and stability of cell resistance contributions and (c) Raman spectrum of the spent cell after 168 h demonstrating the presence of carbon deposits.

Conclusions

In this study, we have demonstrated that *operando* exsolved $FeNi_3$ nanoparticles on SFM-based fuel electrodes are crucial for boosting the performance of ethanol-fueled SOFCs. Doping Ni in SFM (SFMNi) increased surface basicity and oxygen vacancy concentration, thus shifting ethanol steam reforming selectivity toward dehydrogenation compared to SFM. Thermocatalytic experiments revealed that SFMNi exhibits superior ethanol steam reforming activity at 750 °C compared to the undoped SFM sample. The crystallographic and Raman analyses revealed the presence of exsolved $FeNi_3$ nanoparticles on SFMNi, which are highly tolerant to coking. The electrocatalytic evaluation of the samples as fuel electrodes at 750 °C demonstrates that exsolved $FeNi_3$ nanoparticles on the SFMNi fuel electrode enabled double the power densities compared to the SFM electrode due to the higher hydrogen formation rates through ethanol steam reforming. The optimum electrolyte-supported cell with the SFMNi fuel electrode showed considerably stable operation after 168 h (1 week) at 0.212 A cm^{-2} after some hours of stabilisation. These findings exemplify the importance of designing nanoengineered MIEC electrodes with suitable catalytic properties through *operando* exsolution towards enhancing the performance and stability of bioethanol-fueled SOFCs.

Conflicts of interest

There are no conflicts to declare.

Data availability

The authors confirm that the data supporting the findings in this study are available within the article and included as part of the supplementary information (SI).

Supplementary information is available. See DOI: https://doi.org/10.1039/d5cy01572c.

Acknowledgements

The authors acknowledge the financial support from the Brazilian agencies CNEN, CNPq (grants Sis-H2 407967/2022-2, 314801/2025-1 and 446879/2024-0), and FAPESP (grants 2023/14931-8 and 2024/00989-7). Fabio C. Fonseca is a CNPq fellow.

References

1 I. M. Organization, *Fourth IMO GHG Study 2020 Executive-Summary*, 2020.
2 L. van Biert, M. Godjevac, K. Visser and P. V. Aravind, *J. Power Sources*, 2016, **327**, 345–364.
3 Z. A. Che Ramli, J. Pasupuleti, N. F. H. Nik Zaiman, T. S. Tengku Saharuddin, S. Samidin, W. N. R. Wan Isahak, A. G. N. Sofiah, S. K. Kamarudin and S. K. Tiong, *Int. J. Hydrogen Energy*, 2025, **104**, 463–486.
4 F. A. de Bruijn, V. A. T. Dam and G. J. M. Janssen, *Fuel Cells*, 2008, **8**, 3–22.
5 B. van Veldhuizen, L. van Biert, P. V. Aravind, K. Visser and A. Thirumurugan, *Int. J. Energy Res.*, 2023, **2023**, 1–35.
6 A. M. Abdalla, S. Hossain, O. B. Nisfindy, A. T. Azad, M. Dawood and A. K. Azad, *Energy Convers. Manage.*, 2018, **165**, 602–627.
7 S. P. S. Badwal, S. Giddey, A. Kulkarni, J. Goel and S. Basu, *Appl. Energy*, 2015, **145**, 80–103.
8 Y. H. Wan, Y. L. Xing, Y. Xie, N. Shi, J. Xu and C. R. Xia, *ACS Appl. Mater. Interfaces*, 2019, **11**, 42271–42279.
9 N. Sun, F. J. Jin, X. L. Liu, X. W. Liu, J. X. Li, Y. Shen, F. Wang, X. Y. Chu, Z. Wu, J. H. Li and X. L. Lv, *ACS Appl. Energy Mater.*, 2021, **4**, 7992–8002.
10 T. P. Wang, R. Z. Wang, X. Y. Xie, S. Chang, T. Wei, D. H. Dong and Z. Wang, *ACS Appl. Mater. Interfaces*, 2022, **14**, 56735–56742.
11 N. Sun, F. J. Jin, P. C. Wang, T. Chen, Y. H. Ling and S. R. Wang, *J. Power Sources*, 2025, **631**, 236219.
12 N. K. Monteiro, F. B. Noronha, L. O. O. da Costa, M. Linardi and F. C. Fonseca, *Int. J. Hydrogen Energy*, 2012, **37**, 9816–9829.
13 B. Li, J. T. S. Irvine, J. Ni and C. Ni, *Appl. Energy*, 2022, **306**, 118117.
14 S. Zhang, K. Zhu, X. Hu, R. Peng and C. Xia, *J. Mater. Chem. A*, 2021, **9**, 24336–24347.
15 M. C. Steil, S. D. Nobrega, S. Georges, P. Gelin, S. Uhlenbruck and F. C. Fonseca, *Appl. Energy*, 2017, **199**, 180–186.
16 A. A. A. da Silva, M. C. Steil, F. N. Tabuti, R. C. Rabelo-Neto, F. B. Noronha, L. V. Mattos and F. C. Fonseca, *Int. J. Hydrogen Energy*, 2021, **46**, 4309–4328.
17 F. Piazzolla, T. S. Moraes, S. S. Figueiredo, D. F. de Paula, E. L. D. Veiga, C. B. Rodella and F. C. Fonseca, *Catal. Today*, 2025, **444**, 115011.
18 M. S. Khan, S.-B. Lee, R.-H. Song, J.-W. Lee, T.-H. Lim and S.-J. Park, *Ceram. Int.*, 2016, **42**, 35–48.
19 N. Laosiripojana and S. Assabumrungrat, *J. Power Sources*, 2007, **163**, 943–951.
20 A. N. Zainon, M. R. Somalu, A. M. K. Bahrain, A. Muchtar, N. A. Baharuddin, S. A. M. Ali, N. Osman, A. A. Samat, A. Azad and N. P. Brandon, *Int. J. Hydrogen Energy*, 2023, **48**, 20441–20464.
21 Y. G. Guo, S. Wang, R. T. Li, J. C. Yu, X. M. Zhang, M. R. Li, X. S. Zheng, J. F. Zhu, Y. F. Song, G. X. Wang and X. H. Bao, *Joule*, 2024, **8**, 2016–2032.
22 D. Ding, X. Li, S. Y. Lai, K. Gerdes and M. Liu, *Energy Environ. Sci.*, 2014, **7**, 552–575.
23 O. Kwon, S. Joo, S. Choi, S. Sengodan and G. Kim, *JPhys Energy*, 2020, **2**, 032001.
24 D. Neagu, T. S. Oh, D. N. Miller, H. Ménard, S. M. Bukhari, S. R. Gamble, R. J. Gorte, J. M. Vohs and J. T. S. Irvine, *Nat. Commun.*, 2015, **6**, 8120.
25 Y. H. Kim, H. Jeong, B. R. Won, H. Jeon, C. H. Park, D. Park, Y. Kim, S. Lee and J. H. Myung, *Nano-Micro Lett.*, 2023, **16**, 33.
26 Y. H. Li, B. B. Hu, C. R. Xia, W. Q. Xu, J. P. Lemmon and F. L. Chen, *J. Mater. Chem. A*, 2017, **5**, 20833–20842.
27 X. Meng, Y. Wang, Y. Zhao, T. Zhang, N. Yu, X. Chen, M. Miao and T. Liu, *Electrochim. Acta*, 2020, **348**, 136351.
28 Y. Wang, T. Liu, M. Li, C. Xia, B. Zhou and F. Chen, *J. Mater. Chem. A*, 2016, **4**, 14163–14169.
29 Q. A. Liu, X. H. Dong, G. L. Xiao, F. Zhao and F. L. Chen, *Adv. Mater.*, 2010, **22**, 5478–5482.
30 O. Rahumi, M. K. Rath, L. Meshi, I. Rozenblium and K. Borodianskiy, *ACS Appl. Mater. Interfaces*, 2024, **16**, 53652–53664.
31 B.-W. Zhang, M.-N. Zhu, M.-R. Gao, X. Xi, N. Duan, Z. Chen, R.-F. Feng, H. Zeng and J.-L. Luo, *Nat. Commun.*, 2022, **13**, 4618.
32 R. D. Shannon, *Acta Crystallogr., Sect. A*, 1976, **32**, 751–767.
33 D. Papargyriou, D. N. Miller and J. T. Sirr Irvine, *J. Mater. Chem. A*, 2019, **7**, 15812–15822.
34 T. Jardiel, M. T. Caldes, F. Moser, J. Hamon, G. Gauthier and O. Joubert, *Solid State Ionics*, 2010, **181**, 894–901.
35 V. Young and T. Otagawa, *Appl. Surf. Sci.*, 1985, **20**, 228–248.
36 J. Wang, D. N. Mueller and E. J. Crumlin, *J. Eur. Ceram. Soc.*, 2024, **44**, 116709.
37 T. Hou, S. Zhang, Y. Chen, D. Wang and W. Cai, *Renewable Sustainable Energy Rev.*, 2015, **44**, 132–148.
38 F. Polo-Garzon and Z. Wu, *J. Mater. Chem. A*, 2018, **6**, 2877–2894.
39 F. Polo-Garzon and Z. L. Wu, *J. Mater. Chem. A*, 2018, **6**, 2877–2894.
40 G. S. Foo, F. Polo-Garzon, V. Fung, D.-e. Jiang, S. H. Overbury and Z. Wu, *ACS Catal.*, 2017, **7**, 4423–4434.
41 X. Gao, P. Cai, Z. Wang, X. Lv and S. Kawi, *Top. Catal.*, 2022, **66**, 299–325.
42 R. Huang, C. Lim, M. G. Jang, J. Y. Hwang and J. W. Han, *J. Catal.*, 2021, **400**, 148–159.
43 V. Kyriakou, D. Neagu, G. Zafeiropoulos, R. K. Sharma, C. Y. Tang, K. Kousi, I. S. Metcalfe, M. C. M. van de Sanden and M. N. Tsampas, *ACS Catal.*, 2020, **10**, 1278–1288.
44 A. Harbi, A. Azouaoui, S. Benmokhtar and M. Moutaabbid, *J. Supercond. Novel Magn.*, 2022, **35**, 1405–1412.
45 Y. Wu, C. Pei, H. Tian, T. Liu, X. Zhang, S. Chen, Q. Xiao, X. Wang and J. Gong, *JACS Au*, 2021, **1**, 1459–1470.

46 P. Lu, Q. Huang, A. C. Bourtsalas, Y. Chi and J. Yan, *Waste Biomass Valoriz.*, 2017, **10**, 155–165.
47 S. J. Kim and G. M. Choi, *Solid State Ionics*, 2014, **262**, 303–306.
48 Y. Li, X. Chen, Y. Yang, Y. Jiang and C. Xia, *ACS Sustainable Chem. Eng.*, 2017, **5**, 11403–11412.
49 J. R. F. Maring, W. M. Hersbach, S. Zafeiratos, M. C. A. Stuart, A. Banerjee, P. P. Pescarmona and V. Kyriakou, *J. Mater. Chem. A*, 2026, 9543–9556.
50 T. Kato, K. Nozaki, A. Negishi, K. Kato, A. Monma, Y. Kaga, S. Nagata, K. Takano, T. Inagaki, H. Yoshida, K. Hosoi, K. Hoshino, T. Akbay and J. Akikusa, *J. Power Sources*, 2004, **133**, 169–174.
51 M. K. Khameneh and A. Babaei, *Electrochim. Acta*, 2019, **299**, 132–142.
52 S. Primdahl and M. Mogensen, *J. Electrochem. Soc.*, 1999, **146**, 2827–2833.
53 Z. Han, H. Dong, Y. Wu and Y. Yang, *Appl. Surf. Sci.*, 2022, **595**, 153513.
54 D. E. Jiang and E. A. Carter, *Phys. Rev. B: Condens. Matter Mater. Phys.*, 2004, **70**, 064102.
55 P. Tereshchuk and J. L. F. Da Silva, *J. Phys. Chem. C*, 2012, **116**, 24695–24705.
56 S. Zarabi Golkhatmi, M. I. Asghar and P. D. Lund, *Renewable Sustainable Energy Rev.*, 2022, **161**, 112339.

